Grain fragmentation associated continuous dynamic recrystallization (CDRX) of hexagonal structure during uniaxial isothermal compression: High-temperature α phase in TiAl alloys

Fengming Qiang, Emmanuel Bouzy, Hongchao Kou, Yudong Zhang, Lingling Wang, Jinshan Li

Version of Record: https://www.sciencedirect.com/science/article/pii/S0966979520309328
Manuscript_8219625f6eef27ef1aac7eed91d7b005

Grain fragmentation associated continuous dynamic recrystallization (CDRX) of hexagonal structure during uniaxial isothermal compression: high-temperature α phase in TiAl alloys

Fengming Qiang[a,b], Emmanuel Bouzy[b,c,*], Hongchao Kou[a,**], Yudong Zhang[b,c], Lingling Wang[a], Jinshan Li[a]

a State Key Laboratory of Solidification Processing, Northwestern Polytechnical University, 710072, Xi'an, PR China

b Laboratoire d'Etude des Microstructures et de Mécanique des Matériaux (LEM3), UMR CNRS 7239, Université de Lorraine, 57070, Metz, France

c Laboratory of Excellence on Design of Alloy Metals for low-mAss Structures (DAMAS), Université de Lorraine, 57070, Metz, France

Abstract

Dynamic recovery (DRV) and dynamic recrystallization (DRX) of hexagonal materials during hot deformation is a sub-domain of restoration processes, which has not well been addressed. In this work, the DRV and DRX mechanisms of high-temperature α phase in TiAl alloys were thoroughly investigated by microstructural characterization and crystallographic analysis with an extended intragranular misorientation axis (IGMA) analysis method. It was revealed that the nucleation of recrystallized grains experienced three steps: (i) the occurrence of stress-induced grain boundary bulging and the formation of symmetrical-tilt low-angle boundaries characterized by ⟨0001⟩ disorientation axis induced by prismatic <a> slip; (ii) the evolution of the low-angle boundaries into asymmetrical-tilt boundaries characterized by $\langle 10\bar{1}x\rangle$ disorientation axis by local basal <a> slip, or tilt-twist boundaries characterized by $\langle 11\bar{2}y\rangle$ disorientation axis through rotational grain boundary sliding, resulting in the

* Corresponding author.
** Corresponding author.
E-mail addresses: emmanuel.bouzy@univ-lorraine.fr (E. Bouzy), hchkou@nwpu.edu.cn (H. Kou).

formation of subgrains from the boundary bulges; (iii) the detachment of the subgrains and the mixing of the detached subgrains by grain boundary sliding. These three steps happened continuously and repeatedly from the boundary regions toward grain interior till the completion of recrystallization. This work provided original information of continuous DRX (CDRX) of hexagonal materials. The extended IGMA method developed in this study is helpful for related investigations.

Keywords: TiAl alloys; Continuous dynamic recrystallization (CDRX); Grain boundary bulging; Grain fragmentation; Intragranular Misorientation Axis (IGMA) analysis

1. Introduction

Thermomechanical processing is an important technique for metal forming. During the process, crystal deformation and restoration, *i.e.*, recovery and recrystallization, interweave dynamically, resulting in specific microstructural evolution and mechanical property change. Thus, the restoration mechanisms of "dynamic recovery (DRV)" and ''dynamic recrystallization (DRX)" [1–7] have been a subject of intensive study for decades.

Previously, most of the investigations were conducted on the DRX behavior of cubic materials. Discontinuous dynamic recrystallization (DDRX) during which new DRXed grains nucleate and grow at the expense of the work-hardened surroundings has been found to be dominant in FCC materials with low or medium stacking fault energy [8–12]. During the deformation process, bulging of grain boundaries was frequently observed and regarded as a prelude for nucleation. Further analysis revealed that the bulging was operated by a mechanism closely related to the strain-induced grain boundary migration. In such a case, a significant dislocation density difference existed between the front and the behind of the bulged boundary and the migration direction was from the low density region to the high density region [1,13]. Then, a necklace of new grains formed along the boundary [9–12]. However, for BCC metals and FCC metals with high stacking fault energy, continuous

dynamic recrystallization (CDRX) was frequently observed [14,15]. The low angle grain boundaries were formed during deformation by DRV and evolve into high angle grain boundaries through progressive accumulation of dislocations. Necklace microstructure was also produced by CDRX at an intermediate stage owing to the rapid development of strain gradients near grain boundaries [15,16].

For the hexagonal structured materials, such as the Mg alloys, commercially pure Ti (CP-Ti) and TiAl-based alloys (high-temperature α phase) [17], that have drawn considerable industrial attention owing to their light-weight. Due to the limited available slip systems, they should possess specific microstructural characteristics when DRX takes place. The available investigations mainly focused on Mg alloys and CP-Ti. It was found that Mg alloys usually display typical features of CDRX during hot deformation [18–22], i.e., low angle boundaries were introduced due to the accumulation of dislocations, and then new fine grains were developed progressively from grain boundaries to grain interiors with the gradual increase in misorientation at sub-boundaries. Due to the lack of slip systems, twinning [22–26] and kinking [19–22] served as additional mechanisms for rapidly introducing large misorientations in deformation substructures and accelerating the formation of new fine grains. For the DRX behavior of CP-Ti, investigations [27–29] indicated that DRV was the dominant softening process for the annihilation of dislocation during high temperature deformation. The original grain boundaries become serrated with the simultaneous formation of internal subgrains. With further deformation, the microstructure was continuously recrystallized resulting in a fine DRX grain microstructure.

For TiAl alloys, due to the specific Blackburn orientation relationship [30] (Blackburn OR: $\{111\}_\gamma//(0001)_\alpha, \langle 1\bar{1}0\rangle_\gamma//\langle 11\bar{2}0\rangle_\alpha$), the features of the lamellar structure (α_2+γ), such as colony size, lamellar orientation, directly depend on the high-temperature α phase. Therefore, it is necessary to investigate the DRX behavior and its induced microstructure

evolution of the high-temperature α phase during thermomechanical processing. Till now, only several researches [31–33] based on in-situ high-energy X-ray diffraction (HEXRD) characterization technique have been conducted. It has been revealed that the α phase was deformed preferentially by slip than by twinning, and the deformation was superimposed by a relatively slow DRV and a less pronounced DRX process. However, no microstructural evolution information was obtained, and the restoration behavior needs to be further investigated. For the high-temperature α phase in TiAl-based alloys, the situation is different from Mg alloys and CP-Ti, and the investigation is much difficult. On one hand, it is impossible to visualize the microstructures in the required temperature range by in-situ microscopy. On the other hand, because of the narrow single α phase region, the microstructure produced by hot deformation cannot be preserved completely to room temperature even if rapid cooling is performed [34]. It undergoes a phase transformation from α phase to lamellar structure ($\alpha_2+\gamma$) during cooling [17].The dislocation structures produced during hot deformation are destroyed by the formation of the γ lamellae inside the α grains. Fortunately, the $\alpha \rightarrow \alpha_2+\gamma$ phase transformation does not destroy the α grain boundaries and the intragranular low-angle boundaries formed during hot deformation. Therefore, the high temperature deformed microstructure can be reconstructed from the orientation data of the low temperature phase based on the specific phase transformation orientation relationship. The detailed principles and methods have been reported by L. Germain et al. [35] and the techniques have become mature. To reveal the dislocation slip and the formation of the low-angle boundaries evolved from the produced dislocations, the intragranular misorientation axis (IGMA) analysis technique [36–39] has been proved powerful, especially for hexagonal materials with limited active slip systems, and has been successfully applied to analyze the dislocation type in CP-Ti [36] and Mg alloys [37–39]. The main assumption made in the IGMA analysis approach is that under the action of dislocation slip the crystal bends around a

specific crystallographic axis $\boldsymbol{T}$ (termed as ‘‘Taylor axis’’ [39–41]). $\boldsymbol{T}$ is parallel to $(\boldsymbol{b} \times \boldsymbol{n})$, in which $\boldsymbol{b}$ is the dislocation Burgers vector and $\boldsymbol{n}$ the slip plane normal. By this relation, the dominant slip mode in the deformed crystal can be ascertained simply by matching the Taylor axis for a given slip mode to the experimentally determined IGMA. So far, this method has been used in the cases where the deformation involved only one type of dislocation slip. For deformation that involves more types of dislocations or even boundary sliding, the method needs to be extended.

Based on such a situation, we conducted a thoroughly investigation on the DRV and DRX mechanisms of the high-temperature α phase in a TiAl alloy, Ti-44.81Al-3.96Nb-0.98Mo-0.15B (at. %). A simple uniaxial compression was applied to the alloy at 1280 °C where the alloy was composed of single α phase [42]. The hot-compressed microstructures were analyzed based on the electron backscatter diffraction (EBSD) measurement data. The high-temperature α phase was reconstructed using the home-made software, Merengue 2 (as detailed in [35]), based on the measured EBSD data and the Blackburn OR. Furthermore, the IGMA method was extended to analyze the formation mechanisms of asymmetrical-tilt and tilt-twist low-angle boundaries. This study aimed at fully revealing the mechanisms of the DRV and the DRX of the hexagonal phase and developing a relevant analyzing methodology.

2. Experiments

The alloy used in this work is Ti-44.81Al-3.96Nb-0.98Mo-0.15B (at. %). It was fabricated by vacuum arc remelting (VAR) and cast into rods with dimensions of $\emptyset 12$ mm × 180 mm, then hot isostatically pressed (HIP) at 1280 °C for 4 h under a pressure of 140 MPa in argon atmosphere. Cylindrical specimens with dimensions of $\emptyset 10$ mm × 15 mm were cut out of the HIPed cast rods by electric-discharge machining for uniaxial compression experiments. The uniaxial compression experiments were carried out in a Gleeble 3500

simulator under vacuum. The specimens were heated by the Joule effect under a low-frequency current at a rate of 20 °C/s to 1280 ºC, and isothermally held for 10 min, then compressed at a strain rate of 0.01 s^{-1} to the respective true strains of 0.05, 0.07, 0.29 and 1.05. The temperature was controlled by means of type S thermocouples spot-welded directly on the surfaces of the specimens. At the end of the compression, they were water-quenched to preserve the deformed microstructure. To obtain the initial microstructural information before the deformation, one specimen was held isothermally at 1280 ºC for 10 min in a resistance furnace and then water quenched.

The mesoscale microstructures were characterized using a JEOL 6500F scanning electron microscope (SEM) equipped with a field emission gun. The crystallographic features of the microstructures were characterized by EBSD using an Oxford EBSD camera and the Aztec online acquisition software package (Oxford Instruments). To achieve the surface quality for EBSD measurements, the specimens were first mechanically polished then electrolytically polished with a solution of 5% perchloric acid, 35% butan-l-ol and 60% of methanol at 35 V for 10 s at temperatures lower than 5 °C. The EBSD patterns were acquired at the accelerating voltage of 20 kV with a step size of 1 μm for coarse microstructure and a step size of 0.1 μm for fine microstructure. The γ phase was indexed using the tetragonal structure (P4/mmm) parameters. The online orientation determination was assisted with the pseudo-symmetry function [43] incorporated in the Aztec online acquisition software package to secure the reliability and accuracy.

In order to analyze the microstructure characteristics of the high-temperature α phase during compression, the transformed part of the α phase was reconstructed from the low temperature γ phase [35]. After reconstruction, the obtained orientation data of the α phase were analyzed with the Channel 5 (Oxford Instruments) to reveal the features of grain boundaries, substructures and intragranular disorientation. The α grain sizes were determined

based on the reconstructed EBSD data, using the Channel 5 software. Firstly, the grain boundaries were identified under the criterion of that the disorientation angle between neighboring pixels is larger than 15°. Then, the diameter of a circle having equivalent area to that of the grain is defined as the grain size [44]. To ensure a statistical relevance, the grain sizes and the area fractions of grains of interests were determined based on 2 to 4 EBSD maps each covering an area of $1.6 \times 1.2\ mm^2$. Due to the unavoidable phase transformation from the high-temperature α to the γ lamellae that modified the local microstructural constituent, it is difficult to examine the dislocations in the deformed α phase by means of transmission electron microscopy (TEM). The corresponding dislocation activities were analyzed mainly by identifying the disorientation axis of low-angle boundaries and matching the axis with Taylor axes [39–41] listed in Table A2-1 in Appendix 2.

3. Results and Discussion

3.1 Initial microstructure

Fig. 1 (a_1) shows the reconstructed as-thermally-treated α phase (1280 ℃/10 min/water quenching) that was the initial microstructure for the compression. For reference, the original EBSD band quality indexed micrograph demonstrating the γ lamellae formed during cooling within the α grains is displayed in Fig. 1 (a_2). It can be seen from Fig. 1(a_1) that the α grains are in equiaxed shape with an average grain size of 220 ± 84.0 μm. The disorientation angle distribution of the α phase in Fig. 1 (b) is in good agreement with the well-known Mackenzie distribution [45] for materials with random crystal orientations, indicating that the initial α grains do not possess any preferred crystallographic orientations or texture.

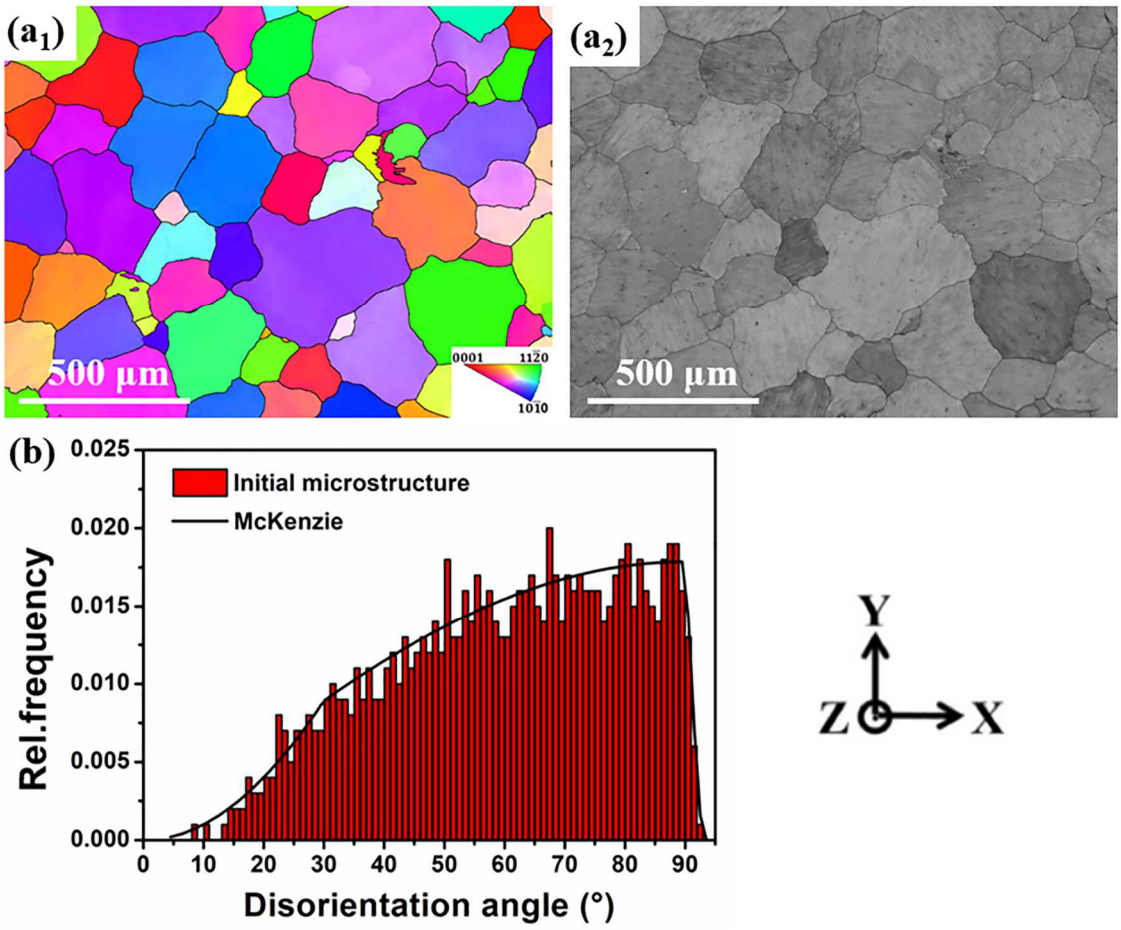

Fig. 1 Initial microstructure. (a_1) EBSD Y axis inverse pole figure (Y-IPF) micrograph of the reconstructed high-temperature α phase; (a_2) EBSD band quality indexed micrograph before reconstruction; (b) disorientation angle distribution of α phase.

3.2 Deformed microstructure

3.2.1 Grain boundary bulging and dynamic recovery (DRV)

Fig. 2 shows the EBSD IPF micrographs of the specimen deformed to the true strain of 0.05 (reconstructed micrograph in Fig. 2 (a_1) and original band quality indexed one in Fig. 2 (a_2)) (The original non-reconstructed micrographs used in the figures hereafter will be given in Appendix 1). It is seen from Fig. 2 (a_1) that although the α grains are still in equiaxed shape, remarkable changes happened to their boundaries. Serrations or bulges appeared along some α grain boundaries, as shown by the two examples outlined with black rectangular in Fig. 2 (a_1).

One can infer that some parts of the grain sheared in one direction and extruded into the neighboring grain, and the other parts were subjected to an "extruding in" from the neighboring grain on the other side. Further local disorientation analysis represented by the Kernel average misorientation (KAM) micrograph displayed in Fig. 2 (b) demonstrates that numerous low-angle disorientations appear along the bulged boundary regions, suggesting that a large number of dislocations were accumulated in front of the bulges. Interestingly, in some locations, the densities of local disorientations inside the bulges are higher than those in front of the bulges, as indicated with the arrows (1 to 4) in Fig. 2 (b). This is opposite to the well-known strain-induced grain boundary migration, where grain boundaries migrate into high dislocation density regions, leaving the region behind with a lower dislocation density [1]. So, in the present work, the boundary bulging should be from a different origin.

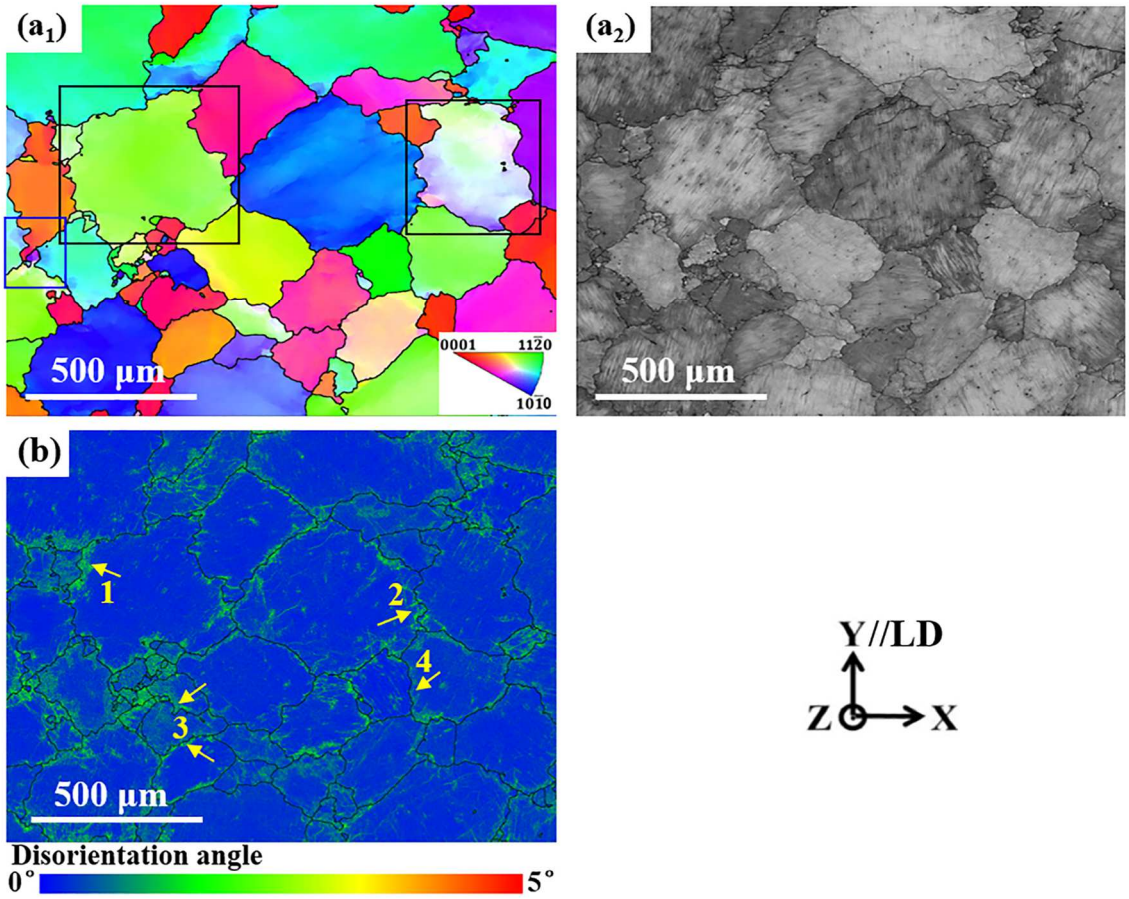

Fig. 2 Deformed high-temperature α microstructure at true strain of 0.05. (a_1) EBSD Y axis inverse pole figure (IPF) micrograph of α phase; (a_2) original EBSD micrograph with band quality indexed contrast. The

black lines stand for grain boundaries and the red lines for the bulged boundaries. (b) Kernel average misorientation (KAM) micrograph of (a_1). In the figures, load direction (LD) is parallel to Y axis (the same below).

To find out the origin behind the boundary bulges, we further analyzed the orientation variation feature near the bulged boundaries. A representative example is shown in Fig. 3 (a). The evolution of the disorientation with respect to the starting point along line L_1 in Grain 1 (G1) from the grain interior (starting point) to the bulged parts is also displayed in the figure. It is seen that the accumulated disorientation angle along L1 exhibits plateaus and jumps (1-3°). The disorientation angles and axes at A, B and C with respect to the orientation of the point before each jump are $1.8°/\langle 000\bar{1}\rangle$, $1.2°/\langle \bar{2}\ 1\ 1\ \overline{12}\rangle$, and $2.4°/\langle 2\ \bar{1}\ \bar{1}\ \overline{12}\rangle$, respectively. The maximum disorientation reaches $5.4°/\langle 000\bar{1}\rangle$ when approaching the boundary. Interestingly, the rotation axes are always close to $\langle 000\bar{1}\rangle$. It is known that among the possible slip modes in the disordered hexagonal α phase [46,47], only the prismatic <a> provides a lattice rotation with the Taylor axis in the $\langle 000\bar{1}\rangle$ direction [36–38,41] (see Table A2-1). This suggests that the deformation was mainly realized by the prismatic <a> slip. With this information, we further examine the relation between the bulge direction and the possible active slip system (slip plane and direction). Then, we plot the pole figures of the prismatic slip plane and the slip direction of G1 and display them in Fig. 3 (b). Among the three prismatic slip variants, the one possessing the highest Schmid Factor, -0.47, for compression is highlighted with the blue circles. This variant was in the favorable orientation to be activated during the deformation. The slip plane trace of this slip variant is also plotted with the black solid line in the $\{1\bar{1}00\}$ pole figure. It is found that the orientation of this trace is in reasonable coincidence with the bulging direction (Line L_1 in Fig. 3 (a)). This suggests that the bulging of the boundary is related to the dislocation movement on this prismatic slip system.

Another microstructural phenomenon near the bulge regions is the formation of the segments of low-angle boundaries as shown by the abrupt change of the colors (marked with the lines at A, B and C) along L1 in Fig. 3 (a), where abrupt disorientation changes are present. This suggests that dislocation rearrangement happened accompanying the deformation. Further trace orientation analysis showed that those low-angle boundaries (lines at A, B and C) in Fig. 3 (a) are oriented very close to the trace of the $\{11\bar{2}0\}$ plane (the red line in the $\langle 11\bar{2}0\rangle/\{11\bar{2}0\}$ pole figure in Fig. 3 (b)). This plane is just perpendicular to the active slip plane, *i.e.*, the $\{1\bar{1}00\}$ plane. Such boundaries, in fact, align with the extra half planes of the prismatic <a> dislocations, as illustrated in Fig. 3 (c). Geometrically, a prismatic <a> edge dislocation is built by an extra half-plane of $\{11\bar{2}0\}$ that intersects the $\{1\bar{1}00\}$ prismatic slip plane on a line of $\langle 000\bar{1}\rangle$ that is the dislocation line, as indicated in Fig. 3 (c). For a low-angle boundary made up of the same type of edge prismatic <a> dislocations aligned normal to the prismatic slip plane, as the case in Fig. 3 (c), the rotation axis between the two parts separated by the boundary is coincident with the $\langle 000\bar{1}\rangle$ direction and the boundary plane is marked by the extra half-planes of the dislocations, *i.e.*, the $\{11\bar{2}0\}$ plane. The situation in Fig. 3 (a) is typical and appears frequently in many other positions in the specimen.

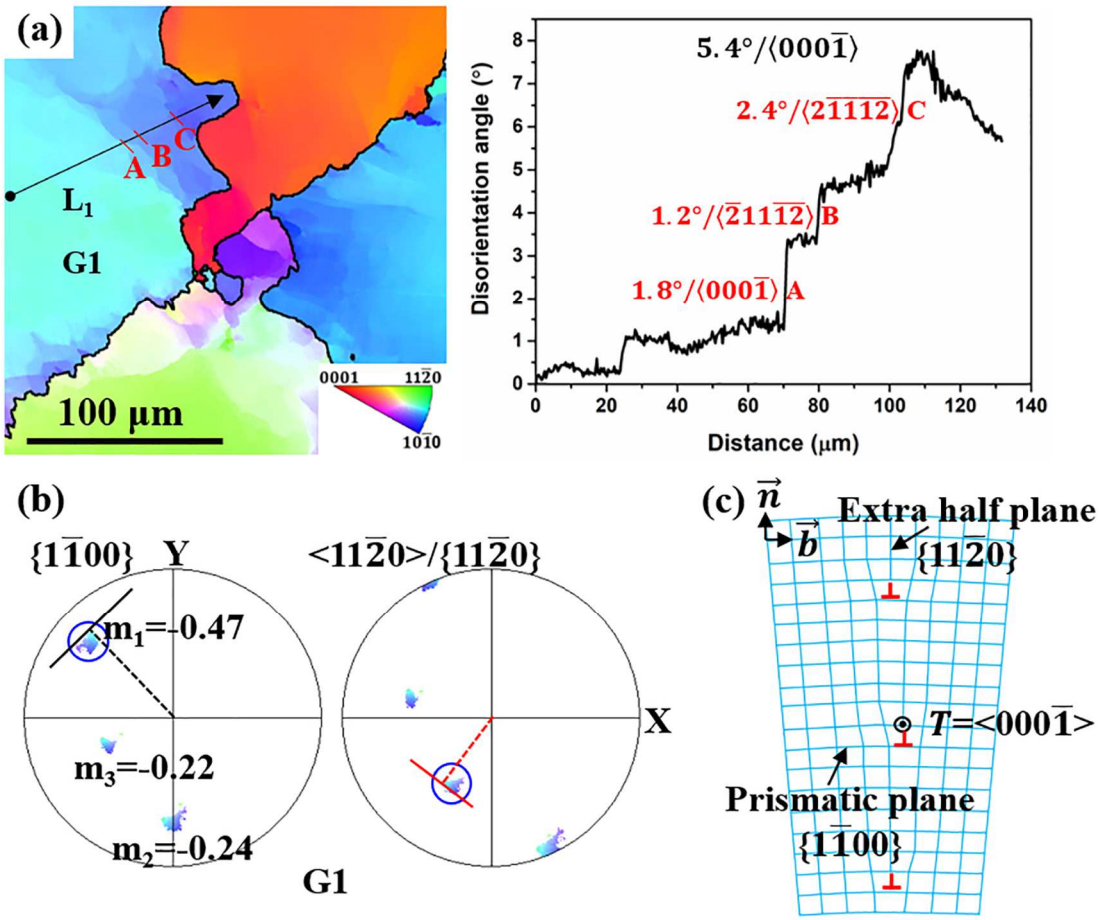

Fig. 3 (a) EBSD Y axis IPF micrograph of a representative example of boundary bulge regions and the correlated disorientations (in angle and axis) along L1 in grain G1. (b) Prismatic slip plane and direction ({1$\bar{1}$00} and <11$\bar{2}$0>) pole figures of G1. (c) Illustration of low-angle boundary formed by edge prismatic <a> dislocations characterized by a rotation around ⟨000$\bar{1}$⟩ and a boundary plane of {11$\bar{2}$0}.

As the small deformation was performed at high temperature, 1280°C (0.85Tm), the atomic bonding is weakened and the vacancy concentration is increased. Thus, the disordered boundary regions could be further extended, i.e., the grain boundaries should be broadened, as illustrated in Fig. 4 (a). When the favorably oriented prismatic slip was activated in the α grains, dislocations of prismatic <a> were generated and moved through the grain interiors and arrived at grain boundary regions (Fig. 4 (b)). The broadened boundaries functioned as dislocation sinks with enhanced free volume. When one dislocation moved out of the grain and annihilated in the boundary, an atomic step of **a** is formed extruding to the boundary

region. When large amount of the same typed dislocations on several bundles of parallel slip planes moved into the boundary region, the boundary becomes microscopically bulged (Fig. 4 (c)). Such a grain boundary bulging mechanism was also evidenced in a hot deformed AZ31 alloy [48].

With the deformation, more dislocations were multiplicated and started to accumulate in front of the grain boundaries, thus, under thermal agitation dislocation climb happened, initiating dislocation rearrangement process and then forming the low-angle boundaries in front of the bulged parts (Fig. 4 (d)). The fact that most of the low-angle boundaries at the present stage (true strain of 0.05) are characterized by a rotation around the $\langle 000\bar{1} \rangle$ axis and the boundary plane coincides with the $\{11\bar{2}0\}$ plane demonstrates that only one prismatic <a> slip was mainly activated and the low-angle boundary is composed of the same type of edge dislocations, as illustrated in Fig. 4 (d). Such boundaries belong to the symmetrical-tilt boundary.

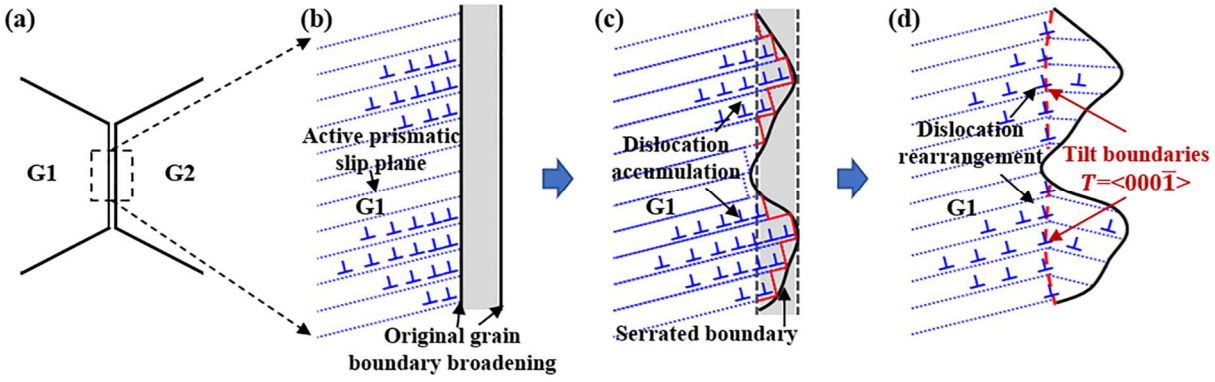

Fig. 4 Schema illustrating the formation of boundary bulging by dislocation slip and the formation of symmetric-tilt low-angle boundary by dynamic recovery (DRV). (a) Grain boundary broadening; (b) activation of dislocation slip and dislocation pile-ups in front of broadened boundary; (c) annihilation of dislocations at grain boundary and formation of boundary bulge; (d) rearrangement of dislocations to form symmetrical-tilt low-angle boundary.

3.2.2 Formation of subgrain

When the true strain was increased to 0.07, almost all the grain boundaries were bulged. Low-angle boundaries ($3-15°$) frequently appeared near triple junctions or grain boundary bulges, as marked with the white lines in Fig. 5 (a). These low-angle boundaries tended to form a closed region with the bulged boundaries, suggesting that subgrains were forming along the bulged grain boundary regions. Detailed orientation analysis of the low-angle boundaries in terms of disorientation angle and the rotation axis in large sample areas (3 EBSD micrographs each covering an area of 1.6×1.2 mm^2) revealed that the disorientation axes of 92.6 % (in number) of low-angle boundaries fall into the following three categories, as also marked in Fig. 5 (a).

(i) $\langle 0001 \rangle$ (39.4%), marked in white in the figure;

(ii) $\langle 10\bar{1}x \rangle$ ($|x| \geq 0$) (32%), marked in black in the figure;

(iii) $\langle 11\bar{2}y \rangle$ ($|y| \geq 0$) (21.2%), marked in yellow in the figure.

The disorientation axis $\langle 0001 \rangle$ are the Taylor axis corresponding to the symmetrical-tilt boundaries formed by the arrangement of the prismatic <a> dislocations. These boundaries are mainly the ones that are not yet totally connected with the original grain boundary to form the subgrains, suggesting that in these regions the DRV is in progress. However, for the low angle boundaries with the disorientation axes of $\langle 10\bar{1}x \rangle$ or $\langle 11\bar{2}y \rangle$, they are usually connected with the bulging boundaries and the enclosed regions possess a much deviated orientation from that of the parent grain, becoming the subgrains separated from the parent grains. To analyze the formation process of the new kinds of boundaries, two representative examples were selected and are displayed in Fig. 5 (b) and (c). In the first case (Fig. 5 (b)), the disorientation between the subgrain and the original grain is $13.99°/\langle \bar{1}011 \rangle$, and in the second case (Fig. 5 (c)), the disorientation is $10.5°/\langle 11\bar{2}1 \rangle$. Analysis revealed that in either case the grain bulging direction (marked with the green lines) is largely consistent with the

trace of one prismatic slip plane, as highlighted with the green lines in the $\{1\bar{1}00\}$ pole figures in Fig. 5 (b) and (c). This indicates that the formation of the low-angle boundaries proceeded by two steps. The first was the formation of a tilt boundary with a disorientation of θ_1/T_1 ($T_1 = \langle 0001 \rangle$) from single prismatic slip and dislocation rearrangement. The second was another rotation θ_2 around T_2 of the bulged part.

The second rotation could be realized by the absorption of the dislocations of another slip system to the yet formed tilt boundaries θ_1/T_1. Thus, using the θ_1/T_1 rotation ($\theta_1 = 1 - 10°$; $T_1 = \langle 0001 \rangle$) as the first rotation and the θ_2/T_2 ($\theta_2 = 1 - 10°$; $T_2 =$ corresponds to Taylor axis of one of the other slip systems in Table A2-1) as the second rotation, we tried to resolve the second one by calculating the total disorientation and then comparing it with the measured disorientation. The second rotation should be the one providing the minimum deviation of the calculated total disorientation from the measured disorientation. The corresponding Taylor axis T_2 reveals the newly activated slip system that contributed to the further evolution of the sub-grain boundaries. The detailed formulation to resolve the second rotation is given in Appendix 2.

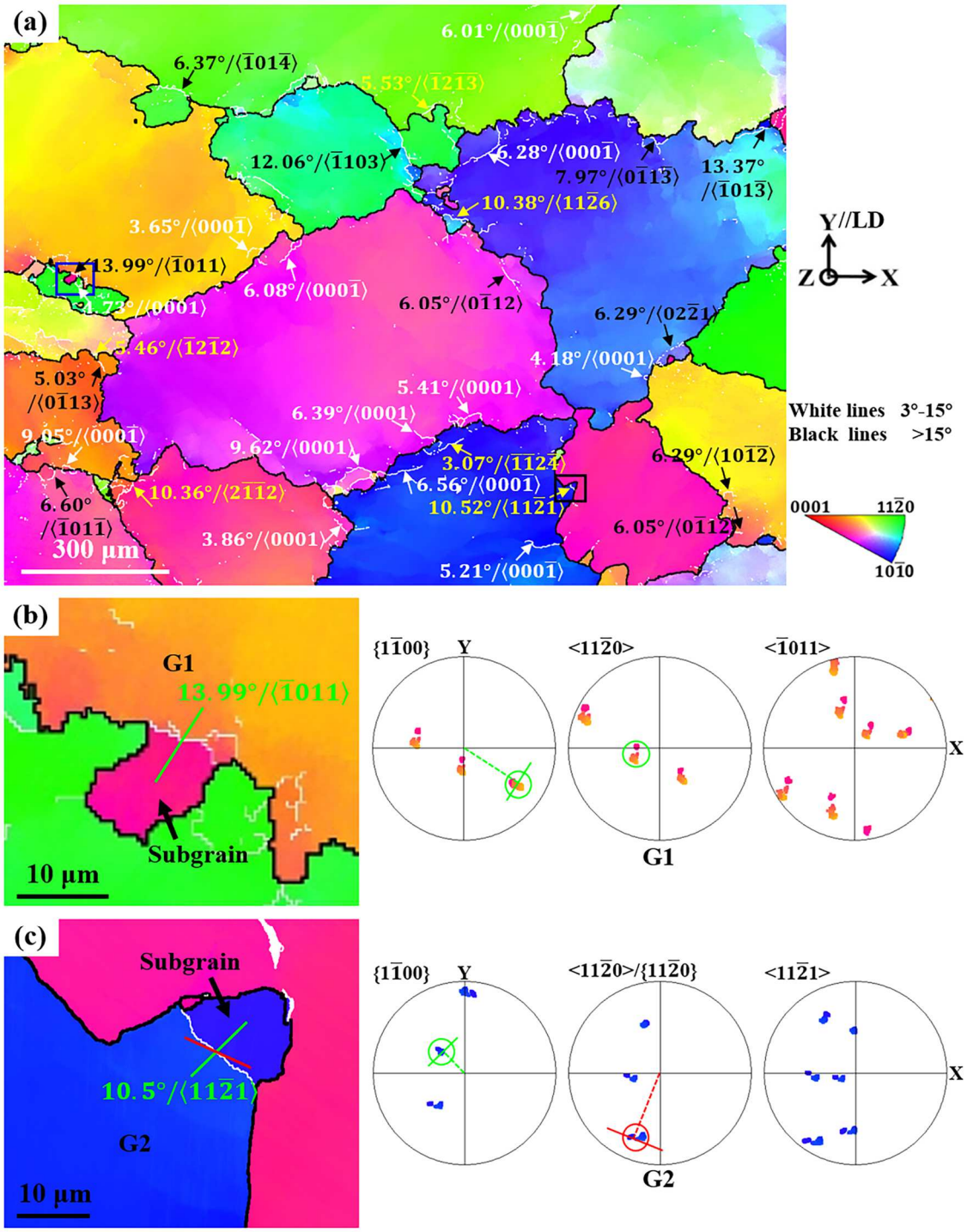

Fig. 5 Microstructural and crystallographic features of α grains in specimen deformed to true strain of 0.07. (a) EBSD Y axis IPF micrograph of high-temperature α phase; (b) EBSD Y axis IPF micrograph of the area outlined with blue rectangle in (a), and pole figures of prismatic slip plane and direction ($\{1\bar{1}00\}$ and $\langle 11\bar{2}0\rangle$) and the disorientation axis $\langle \bar{1}011\rangle$ in G1; (c) EBSD Y axis IPF micrograph of the area outlined with black rectangle in (a), and pole figures of prismatic slip plane and direction ($\{1\bar{1}00\}$ and $\langle 11\bar{2}0\rangle$) and the disorientation axis $\langle 11\bar{2}1\rangle$ in G2.

The calculation results show that for the $T = \langle 10\bar{1}x \rangle$ boundaries, the second rotation axis T_2 is $\langle 10\bar{1}0 \rangle$, corresponding either to a basal <a> slip or a pyramidal II <c+a> slip (Table A2-1). More examples with disorientation axis of $\langle 10\bar{1}x \rangle$ are displayed in Table A2-3 in Appendix 2. The occurrence of the basal slip is more probable because the CRSSs of prismatic, basal and pyramidal slip are ordered increasingly from the prismatic to the pyramidal slip [47,49]. The basal slip has lower CRSS than the pyramidal slip, thus, under specific local stress, the basal slip could easily be activated. Further analysis show that the Schmid factors of the activated basal slip are not always very high. Even in some grains, all the absolute values of the Schmid factors of the basal slip is smaller than 0.3, indicating that the activation was mainly driven by local incompatible deformation between the neighboring grains in the boundary regions. These results confirmed that the appearance of the $\langle 10\bar{1}x \rangle$ low-angle boundaries was indeed realized by two steps. The first is the formation of the symmetrical tilt low-angle boundaries with disorientation axis of <0001> by the rearrangement of the prismatic <a> dislocations, and the evolution of the symmetrical tilt boundaries to the asymmetrical low-angle boundaries by absorption of the basal <a> dislocations, as illustrated in Fig. 6 (a).

However, for the $T = \langle 11\bar{2}y \rangle$ boundaries, we tried the Taylor axis of all the possible slip systems in hexagonal structures, but could not find a reasonable match between the calculated total rotation and the measured disorientation. This means that the second rotation was not realized by dislocation activity but by a different mechanism. Thus, we further examined the orientation of the boundary plane. Interestingly, we found that although the disorientation axis of the boundaries was no longer $\langle 0001 \rangle$, the trace of the low-angle boundary (in white) is very close to the trace of the $\{11\bar{2}0\}$ plane, as indicated with the red line in the IPF micrograph and in the $<11\bar{2}0>/\{11\bar{2}0\}$ pole figure in Fig. 5 (c). It means that the boundary plane still remained the $\{11\bar{2}0\}$ plane. As analyzed above (Fig. 3 (c)), this plane corresponded

to the extra half-plane of the edge prismatic <a> dislocations formed during the first step, inferring that during the second step the evolution of the boundary could only be realized by a rotation around the axis normal to the low-angle boundary formed in the first step, *i.e.,* <11$\bar{2}$0> axis. Thus, using $T_2 = \langle 11\bar{2}0 \rangle$ as the second rotation axis to calculate the total rotation, good matches appeared between the calculated dislocations and the measured ones, confirming that the second rotation was indeed realized by a rotation around the axis normal to the boundary. More examples with disorientation axis of $\langle 11\bar{2}y \rangle$ are displayed in Table A2-4 in Appendix 2. This result evidenced that at the present stage of deformation grain boundary sliding happened through which the tilt symmetrical low-angle boundaries further evolved into the tilt-twist boundaries, as illustrated in Fig. 6 (b). As the sliding is rotational, we can denote such boundary sliding by rotational boundary sliding. By these two ways, the orientations of bulged parts continuously deviated from those of original grains, initiating the formation of the subgrains.

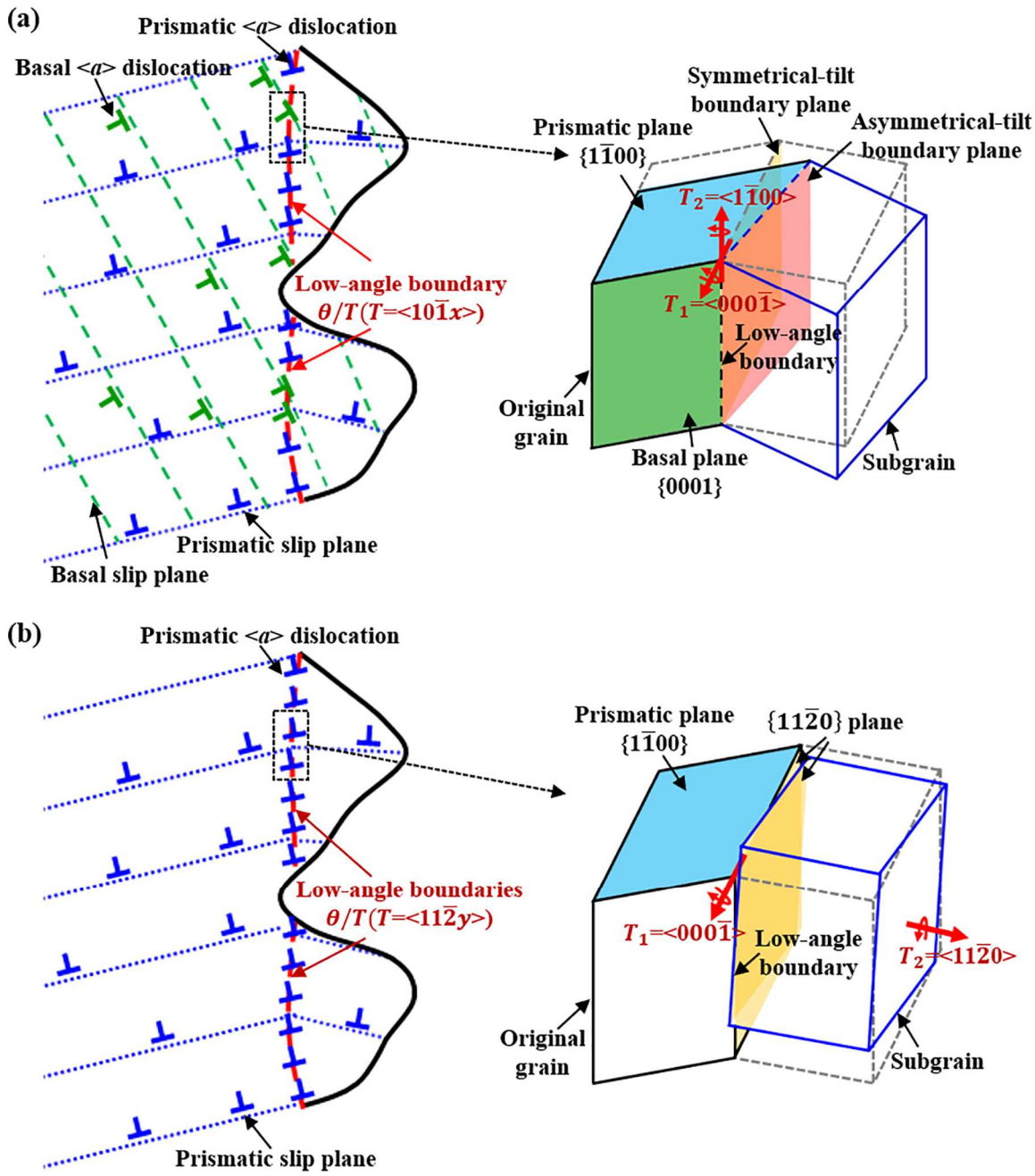

Fig. 6 Schema illustrating the evolution of low-angle boundaries with further deformation. (a) Asymmetrical-tilt boundaries with disorientation of θ/T ($T = \langle 10\bar{1}x\rangle$) formed by the first rotation θ_1/T_1 ($T_1 = \langle 000\bar{1}\rangle$) and the second rotation θ_2/T_2 ($T_2 = \langle 1\bar{1}00\rangle$); (b) tilt-twist boundary with the disorientation of θ/T ($T = \langle 11\bar{2}y\rangle$) formed by the first rotation θ_1/T_1 ($T_1 = \langle 0001\rangle$) and the second rotation θ_2/T_2 ($T_2 = \langle 11\bar{2}0\rangle$).

3.2.3 Grain growth

It should be mentioned that accompanying grain boundary bulging grain growth occurred during the deformation (up to ε=0.07). From the data given in Table 1, one can see that the average grain size increased from initially 220±84.0 μm (ε=0) to 326±160.2 μm when the specimen was deformed to ε=0.05, and further to 580±216.3 μm when the strain went up to ε=0.07. Interestingly, the values of the standard deviation were nearly doubled at ε=0.05 and almost tripled at ε=0.07. This indicates that the grain size distribution is very large. As at these two deformation stages, recrystallized grains did not form numerously, the wide grain size spread infers that grain growth was not uniform. This phenomenon is related to the early state of hot deformation. As at the two tiny strains, the imposed deformation was not unanimously dispatched to every grain. Some grains possessing favorably oriented slip systems were deformed, but the others without favorably oriented slip systems were less deformed or not deformed. For the former, boundary bulges were formed as a result of deformation. For the latter, the high compression temperature became the most important factor to promote grain boundary migration. Thus, certain grains grew by consuming the others, which resulted in the heterogeneous grain size distribution.

Table 1 α grain size and area fractions of grains of interest of the specimens with different true strains

True strain ε	**Retained coarse grains**		**Newly-formed grains**	
	Average size (μm)	Fraction (%)	Average size (μm)	Fraction (%)
0	220±84.0	100	/	0
0.05	326±160.2	100	/	0
0.07	580±216.3	95.5	12±6.3	4.5
0.29	490±284.5	64.4	26±11.4	35.6
1.05	/	0	45±23.9	100

3.2.4 Continuous dynamic recrystallization (CDRX)

3.2.4.1 Necklace structure

Fig. 7 is the microstructure of the specimen deformed to the true strain of 0.29. It can be clearly seen that the microstructure exhibits bimodal grain structure, composed of the newly formed small grains and the remnants of the initial coarse grains (Fig. 7 (a)). The newly formed small grains with an average size of about 26 ± 11.4 μm (Table 1) are distributed along the initial grain boundaries, forming a necklace structure. When the strain increased from 0.07 to 0.29, the grain size of the retained coarse grains decreased, from an average size of 580 ± 216.3 μm to an average size of 490 ± 284.5 μm, and the area fraction of the small grains increased from 4.5% to 35.6% (Table 1). The KAM micrograph displayed in Fig. 7 (b) shows that the newly formed small grains indicated by the yellow arrows possess much less amount of local disorientations, thus, these small grains possess the feature of recrystallized grains. This suggests that the recrystallization process was realized by a continuous detachment of the subgrains from the grain boundary regions, and such a process occurred repeatedly toward grain interiors, demonstrating a CDRX feature. From the color features of the small grains along the coarse grain boundary regions in Fig. 7 (a), one can see that the small grains detached from the two neighboring coarse grains were further mixed during the deformation process.

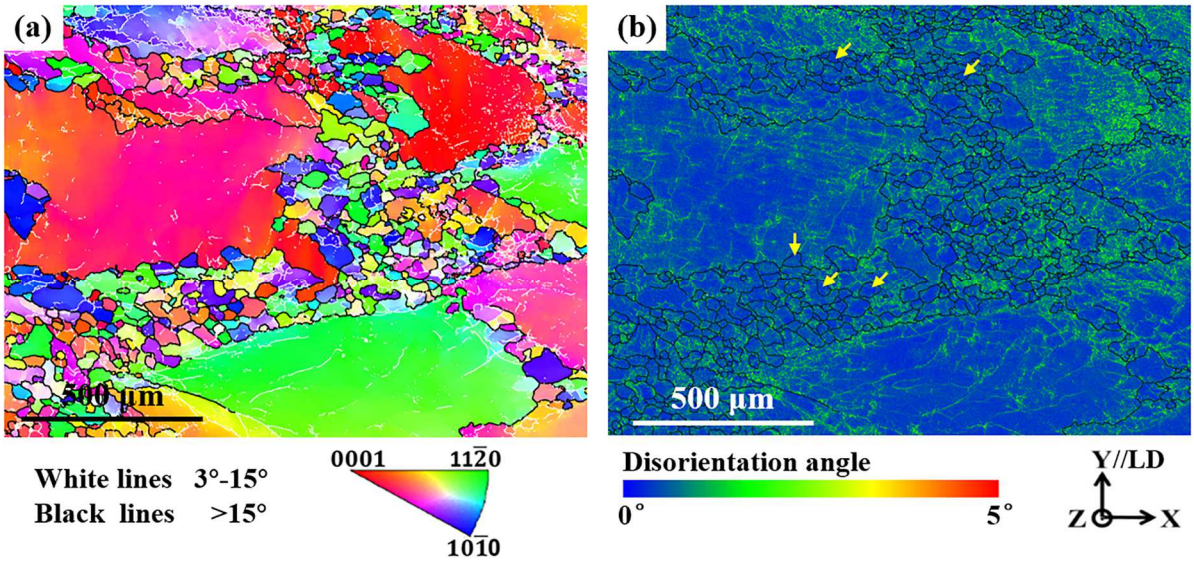

Fig. 7 Micrographs of the α phase in the specimen deformed to the true strain of 0.29. (a) EBSD Y axis IPF micrograph; (b) KAM micrograph.

To reveal the mechanism of the mixing process of the recrystallized grains, the crystallographic orientation features of two examples of necklace areas, the one with a few small grains representing the beginning of detachment and the other with some more small grains representing the penetrating of the small grains into neighboring small grain regions displayed in Fig. 8, were further analyzed. It is seen from Fig. 8 (a) that the two coarse grains with distinct orientations (represented by the {0001} and {10$\bar{1}$0} pole figures) were separated by a layer of small sized domains delimitated either by high-angle boundaries (black lines) or low-angle boundaries (white lines) or the mix of the two. This suggests that for these two coarse grains the formation of the "necklace" just started. Although the small domains were separated from the neighboring coarse grains by boundaries with disorientation angles higher than 15°, their orientations are characteristically either close to G1 or to G2. For example, in the EBSD IPF micrograph in Fig. 8 (a), the orientations of domains D1 and D2 (enclosed in the blue and black squares in the pole figures) are close to that of G1 and those of domains D3 and D4 (enclosed in the red and green circles in the pole figures) are close to that of G2.

Clearly these orientation domains were detached from the two coarse grains (G1 and G2) and mixed in the necklace layer. For the case shown in Fig. 8 (b), the thick "necklace" layer was formed around the coarse red grain. The $\{0001\}$ and $\{1\bar{1}00\}$ pole figures in Fig. 8 (b) are from the small red domains and the coarse red grain in the EBSD Y axis IPF micrograph. One can see that the small red domains possess close crystallographic orientations to that of the coarse red grain. However, the small red domains were already separated by layers of small domains detached from the other neighboring coarse grains. This suggests that grain boundary sliding between the detached small domains happened, resulting in the mixing of these small grains. In this case the boundary sliding is both translational and rotational. The former allows the detached grains to spatially separate from their parent grain but does not affect their orientation. The latter is opposite. It does not make spatial separation but deviates their orientations from those of the parent. The evidence of the spatial separation of the new grains from the parent grain and their orientation deviation from the parent orientation infers the existence of the two types of boundary sliding. The occurrence of grain boundary sliding is quite reasonable under the present deformation conditions. Firstly, the deformation temperature (1280°C) was very high ($0.8T_m$), thus grain boundary strength was very low. Secondly, the deformation strain rate was relatively low (0.01 s^{-1}) that offered a sufficient time window for the slow process of sliding to occur, Thirdly, the sizes of the detached domains were relatively small that provided a high amount of boundary area. All these factors favored the occurrence of grain boundary sliding. This mechanism should also be an important deformation mechanism for the small grains to contribute to the external deformation and allow the spatial separation of the detached grains from their parent grains.

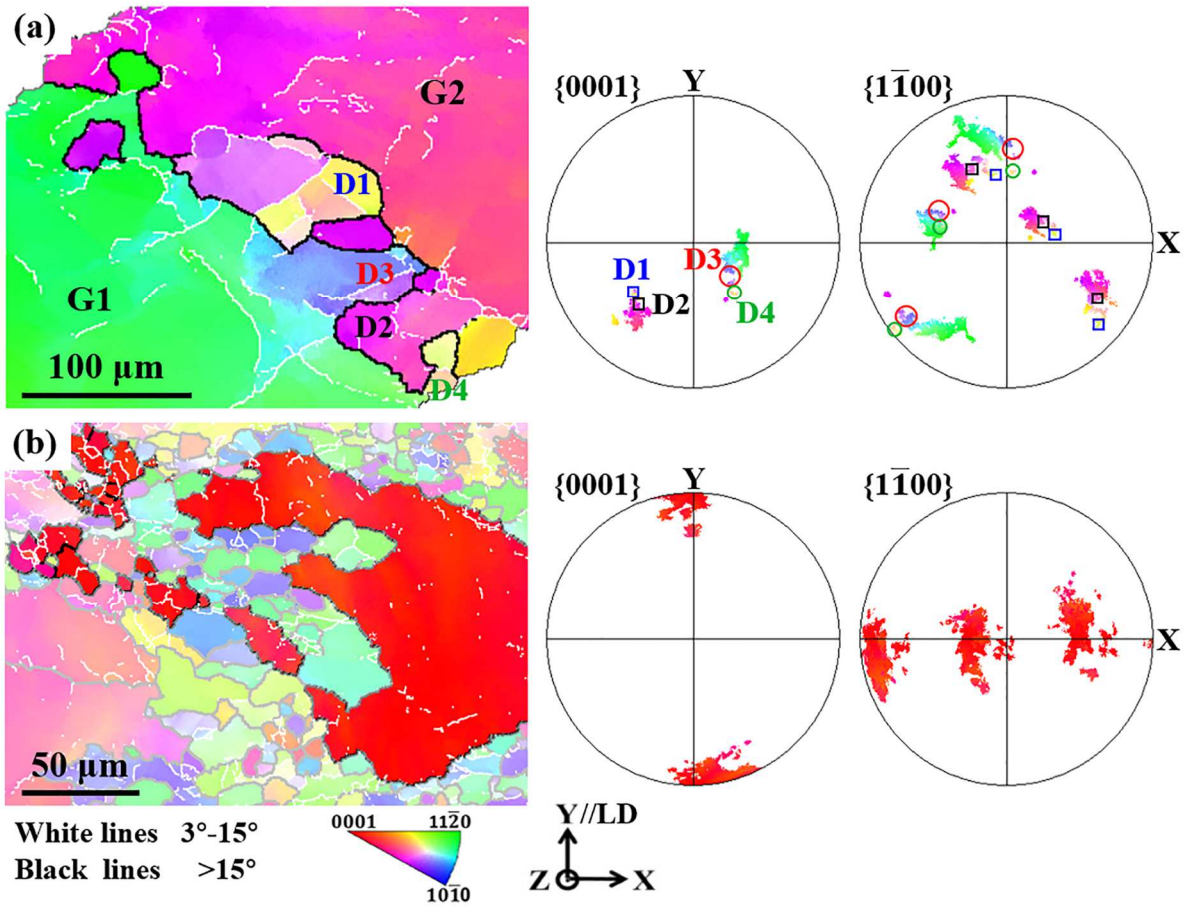

Fig. 8 EBSD Y axis IPF micrographs and the corresponding {0001} and {10$\bar{1}$0} pole figures of the grains in two necklace regions. (a) Necklace region with less small grains representing the beginning of grain detachment; (b) necklace region with more small grains representing the mixing of small grains. The poles in the pole figures in (b) are from the coarse red grain and the small red domains.

3.2.4.2 Completion of CDRX

Fig. 9 displays the EBSD micrograph of the specimen deformed to the true strain of 1.05. It can be seen that the microstructure is mainly composed of nearly equiaxed small grains, indicating the completion of the recrystallization process. The average grain size is about 45 ± 23.9 μm. However, it is worth mentioning that in some relatively large grains there exist segments of high-angle boundaries connected with segments of low-angle boundaries, as marked with the black arrows in Fig. 9. This suggests that the grain fragmentation process

was still in progress. The low-angle boundaries would further evolve into high-angle boundaries and eventually divided the coarse grains into differently oriented small grains.

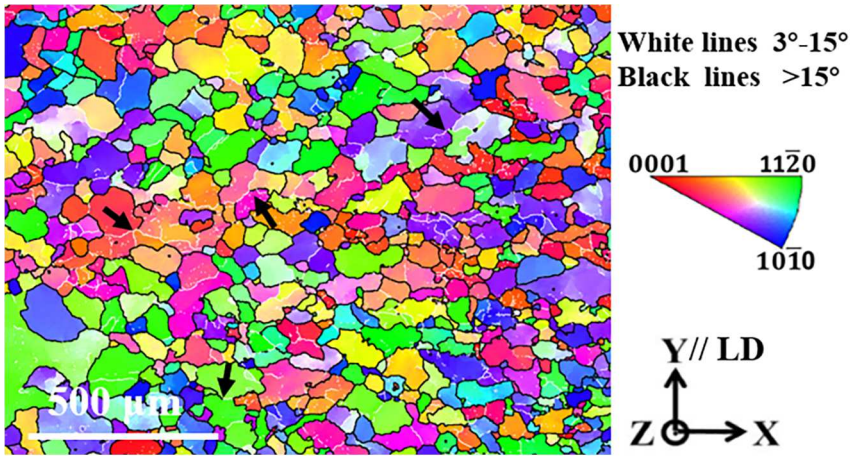

Fig. 9 EBSD Y axis IPF micrograph of the specimen deformed to the true strain of 1.05.

Although the nucleation of the recrystallized grains in the present work also started from subgrains as the recrystallized nuclei, it is quite different from the commonly reported nucleation modes related to subgrains, *i.e.*, nucleation by sub-boundaries migration and nucleation by subgrain coalescence [50]. There was neither subgrain boundary migration nor subgrain coalescence, but subgrain detachment from the parent grains by the increasing disorientation and grain boundary sliding. In consequence, the nuclei formed in this way were very large with sizes of several tens of micrometers and the recrystallization did not obviously undergo the grain growth stage. The recrystallization progressed (with the deformation) rather by continuous repetition of the formation of the subgrains and the detachment of the subgrains from grain boundary bulges, which developed from grain boundary region toward grain interior until all the initial coarse grains were fragmented. Such a feature should be related to the lack of slip systems of hexagonal crystals and also the slow deformation condition of the present work. During the deformation, only one or two slips systems were activated. On one hand, the produced dislocations could smoothly move to grain boundary regions without much hindrance, and on the other hand, no dislocation entanglement could occur in the grain interiors to form intragranular subgrains. As the subgrains is formed preferentially at the

boundary regions, grain boundary sliding is much easier than in grain interiors. Thus, subgrain detachment (especially translational sliding) prevailed over sub-boundaries migration and subgrain coalescence.

4. Summary

The mechanisms of DRV and CDRX of high-temperature α phase in a Ti-44.81Al-3.96Nb-0.98Mo-0.15B (at. %) alloy under a uniaxial isothermal compression at 1280 ℃ were thoroughly investigated by means of microstructural and crystallographic analysis with an extended IGMA analysis method. The formation of the recrystallized nuclei can be categorized into three characteristic stages, *i.e.*, grain boundary bulging with the formation of symmetrical-tilt boundaries near boundary bulging regions, subgrain formation at bulged boundary regions by evolving symmetrical-tilt boundaries into asymmetrical-tilt or tilt-twist boundaries and the formation of recrystallized grain by subgrain detachment from the parent grain.

During the first stage, the favorable prismatic slip systems were activated. Edge prismatic <a> dislocations were generated and piled up near grain boundaries. Under the unidirectional compression, grain boundaries that were not normal to the compression axis were broadened due to the tension in the direction perpendicular to the compression axis. Dislocations were annihilated in the broadened boundary and formed steps bulging into the neighboring grains, resulting in bulging boundaries. Due to thermal agitation, accumulated dislocations also rearranged by dislocation climb accompanying the boundary bulging. Symmetrical-tilt boundaries characterized by a disorientation axis of <0001> were formed. When the deformation progressed to the second stage, the formed symmetrical-tilt boundaries further evolved in two different ways. The one was by absorbing basal <a> dislocations formed due to incompatible deformation between neighboring grains in the bulged boundary regions, which transformed the symmetrical-tilt boundaries into asymmetrical-tilt boundaries

characterized by a rotation around $\langle 10\bar{1}x\rangle$. The other was by a rotational movement of the bulged parts around the normal axis of the symmetrical-tilt boundary (rotational sliding), which transformed the symmetrical-tilt boundary into a tilt-twist boundary characterized by a rotation around $\langle 11\bar{2}y\rangle$. This resulted in the formation of the subgrains from the bulged grain boundary regions. When the deformation progressed to the third stage, the formed subgrains are detached from the parent grains and mixed with the ones detached from the neighboring grains by boundary sliding. Such a nucleation process from subgrain formation is also different from the classical subgrain growth by boundary migration or subgrain growth by coalescence. The three processes repeatedly happened from grain boundary regions toward grain interiors until the whole initial microstructure was replaced by the recrystallized grains.

The results of the present work provided original information of the CDRX of hexagonal structured materials. The extended IGMA analysis method developed in the present study is applicable to the related investigations on deformation behavior of high-temperature phases when dislocations could not be preserved to room temperature.

Acknowledgements

This work was supported by the National Natural Science Foundation of China under grant No. 51571162, and the Research Found of the State Key Laboratory of Solidification Processing (NWPU), China under grant No. 2020-TZ-03. The first author Fengming Qiang is grateful to the China Scholarship Council for the support to her PhD study in France. The authors acknowledge the inventors of the Merengue 2 for the reconstruction of high-temperature α phase in the present work.

Appendix 1: Original EBSD micrographs with band quality indexed contrast

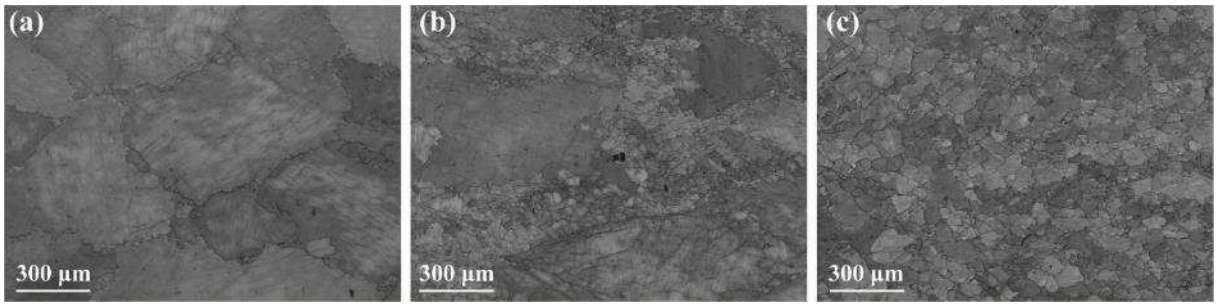

Fig. A1 Original EBSD micrographs with band quality indexed contrast of the specimens deformed to true strains of (a) 0.07, (b) 0.29, and (c) 1.05.

Appendix 2: Extended Intragranular Misorientation Axis (IGMA) analysis

In this appendix, an extension of the Intragranular Misorientation Axis (IGMA) analysis to complex cases is presented where different slip modes or even slip and grain boundary sliding are both activated in a grain. The IGMA analysis allows to determine the dominant slip system inside a grain by matching the theoretical rotation axis (Taylor axis) for a given slip system to those of the geometrically necessary dislocation (GND) forming the low-angle boundaries in a deformed grain. This analysis method works well for hexagonal materials of which only a few slip systems are available and often one is dominant. The theoretical Taylor axes have been calculated for different slip modes in hexagonal materials (see Table A2-1). Below, the analysis method is extended, in addition to the primary slip mode, to identify a secondary slip mode or a rotational grain boundary sliding.

We assume that the disorientation (θ/T: θ rotation angle and T rotation axis) associated to a low-angle boundary constituted of dislocations, can be decomposed into several single or basic disorientations each characterized by a specific rotation axis. The basic disorientations are either from symmetrical-tilt boundaries made of dislocations with the same Burgers vector

and the rotation axis is the so-called Taylor axis, as listed in Table A2-1, or from rotational boundary sliding around the axis normal to the boundary, as listed in Table A2-2. For clarity and simplicity, we suppose that θ/T is composed of two single rotations, θ_1/T_1 and θ_2/T_2 (Fig. A2-1 (a)). Thus the following relation in matrix notation of the rotations holds:

$$G = S_i \cdot G_1 \cdot S_j \cdot G_2, \tag{A2-1}$$

where G, G_1 and G_2 are the rotational matrices representing the misorientation of θ/T, θ_1/T_1 and θ_2/T_2, as illustrated with the flow chart in Fig. A2-1 (b), and S_i and S_j the ith and jth rotational symmetry matrices of the crystal structure. The rotational matrix of G can be calculated using the rotation angle θ and the unit rotation axis $T(d_1, d_2, d_3)$ as follows:

$$G = \begin{bmatrix} (1-{d_1}^2)\cos\theta + {d_1}^2 & d_1d_2(1-\cos\theta) - d_3\sin\theta & d_1d_3(1-\cos\theta) + d_2\sin\theta \\ d_1d_2(1-\cos\theta) + d_3\sin\theta & (1-{d_2}^2)\cos\theta + {d_2}^2 & d_2d_3(1-\cos\theta) - d_1\sin\theta \\ d_1d_3(1-\cos\theta) - d_2\sin\theta & d_2d_3(1-\cos\theta) + d_1\sin\theta & (1-{d_3}^2)\cos\theta + {d_3}^2 \end{bmatrix}, \tag{A2-2}$$

By knowing any of two rotations, the remaining rotation can be resolved. This formulation can be readily extended to a rotation composed of multiple single rotations.

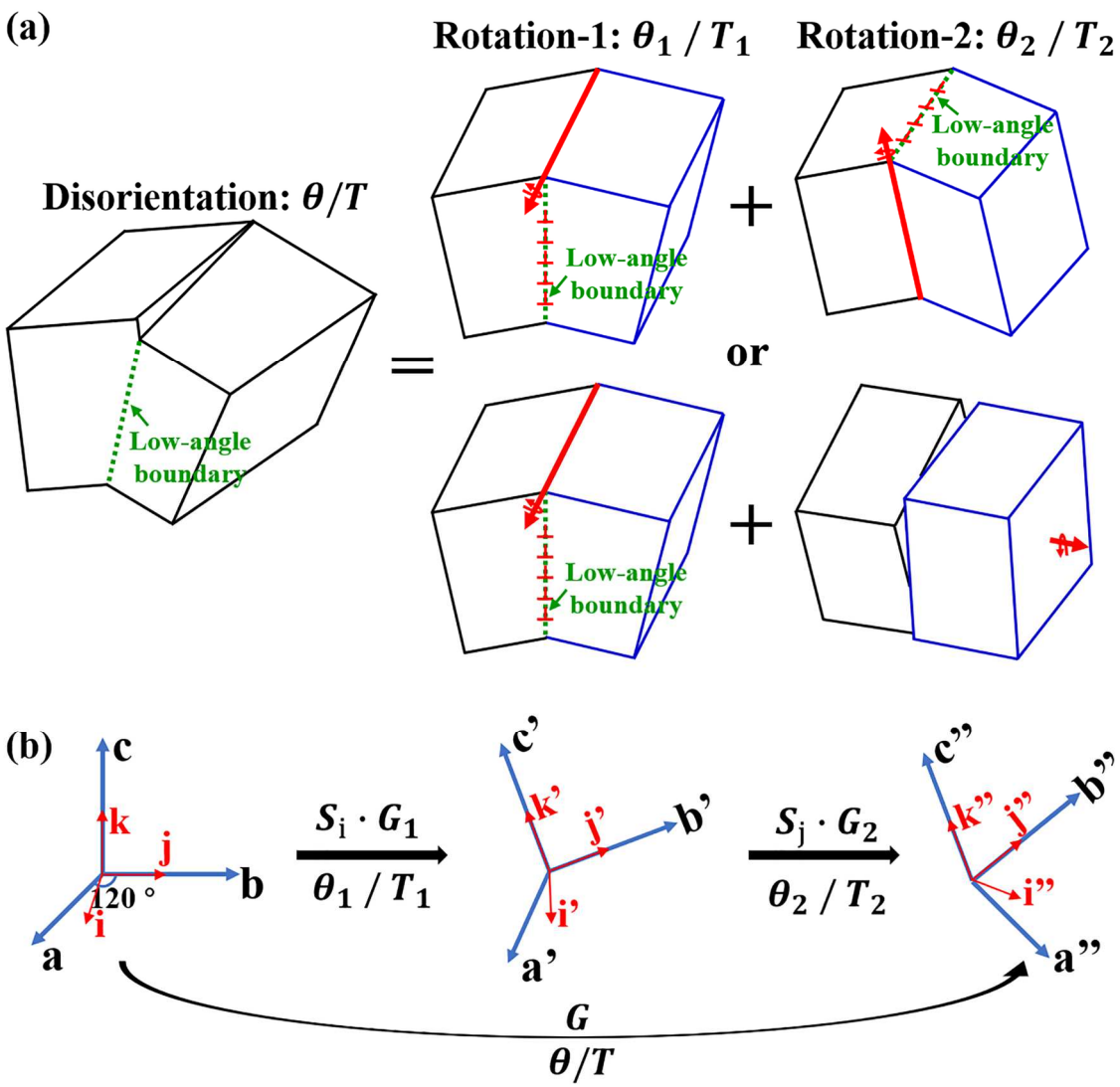

Fig. A2-1 (a) Schema illustrating the decomposition of the low-angle boundary into two symmetrical tilt boundaries made of dislocation with two different Burgers vectors or into one symmetrical-tilt boundary and a rotational sliding around the axis normal to the extra-half plane of the dislocation of symmetrical-tilt boundary; (b) schema showing the corresponding crystallographic rotations.

Now we use the two characteristic rotations found in the present work to illustrate the analysis procedure. The first case corresponds to the low-angle boundaries featured by a rotation around $\langle 10\bar{1}x \rangle$ and the second to the low-angle boundaries featured by a rotation around $\langle 11\bar{2}y \rangle$. In the two cases, the first rotation is θ_1/T_1 ($T_1 = \langle 0001 \rangle$) and we assume that θ_1= 1 to 10°. Supposing that the second rotation T_2 corresponds to a Taylor axis of another

slip system (as listed in Table A2-1) or to the axis normal to the extra half-plane of the corresponding boundary dislocations (as listed in Table A2-2), and θ_2= 1 to 10°. The total rotation $G\ (\theta/T)$ can be calculated. Then the calculated G is further compared with the measured $G^{ex}\ (\theta/T)^{\mathrm{ex}}$, the θ_2/T_2 provides the smallest deviation ($\Delta\theta$) from the experimental $G^{ex}\ (\theta/T)^{\mathrm{ex}}$ is assessed as the second rotation.

Table A2-1 Possible slip modes in disordered α-Ti3Al (c/a=1.60) and the corresponding Taylor axes

Slip mode	Slip type	Taylor axis
$\{1\bar{1}00\}\langle11\bar{2}0\rangle$	Prismatic $\langle a\rangle$	$\langle000\bar{1}\rangle$
$\{0001\}\langle11\bar{2}0\rangle$	Basal $\langle a\rangle$	$\langle1\bar{1}00\rangle$
$\{10\bar{1}1\}\langle1\bar{2}10\rangle$	Pyramidal $\langle a\rangle$	$\langle\bar{1}012\rangle$
$\{10\bar{1}1\}\langle11\bar{2}\bar{3}\rangle$	Pyramidal-I $\langle c+a\rangle$	$\langle27\ 44\ \overline{17}\ 10\rangle$
$\{11\bar{2}2\}\langle11\bar{2}\bar{3}\rangle$	Pyramidal-II $\langle c+a\rangle$	$\langle1\bar{1}00\rangle$

Table A2-2 Slip modes in disordered α-Ti3Al (c/a=1.60) and the axis normal to the extra-half plane of dislocation

Slip mode	**Extra half plane / Symmetrical-tilt boundary plane**	**Rotation axis of grain boundary sliding**
$\{1\bar{1}00\}\langle11\bar{2}0\rangle$	$\{11\bar{2}0\}$	$\langle11\bar{2}0\rangle$
$\{0001\}\langle11\bar{2}0\rangle$	$\{11\bar{2}0\}$	$\langle11\bar{2}0\rangle$
$\{10\bar{1}1\}\langle1\bar{2}10\rangle$	$\{1\bar{2}10\}$	$\langle1\bar{2}10\rangle$
$\{10\bar{1}1\}\langle11\bar{2}\bar{3}\rangle$	$\{5\ 5\ \overline{10}\ \overline{26}\}$	$\langle11\bar{2}\bar{3}\rangle$
$\{11\bar{2}2\}\langle11\bar{2}\bar{3}\rangle$	$\{5\ 5\ \overline{10}\ \overline{26}\}$	$\langle11\bar{2}\bar{3}\rangle$

For the first case, the low-angle boundaries with disorientation axes of $\langle10\bar{1}x\rangle$, $T_2 = \langle10\bar{1}0\rangle$ provides the smallest deviation ($\Delta\theta$) of the calculated $G\ (\theta/T)$ from the experimental $G^{ex}\ (\theta/T)^{\mathrm{ex}}$. The results of several examples are displayed in Table A2-3. For the second case, the low-angle boundaries with disorientation axis of $\langle11\bar{2}y\rangle$, $T_2 = \langle11\bar{2}0\rangle$ offers the smallest $\Delta\theta$. The results of several examples are displayed in Table A2-4.

Table A2-3 Calculation results for low-angle boundaries with disorientation axis around $\langle10\bar{1}x\rangle$.

Experimental result $G^{ex}\ (\theta/T)^{\mathrm{ex}}$	T_1	T_2	**Calculated result** θ_1	θ_2	$G\ (\theta/T)$	$\Delta\theta$

$6.37°/\langle\bar{1}01\bar{4}\rangle$			5.6°	3.0°	$6.3524°$ $/\langle\overline{0.4579}\ \overline{0.0266}\ 0.4845\ \overline{1.9040}\rangle$	0.1502
$12.06°/\langle\bar{1}103\rangle$			9.8°	7°	$12.0383°$ $/\langle\overline{0.5505}\ 0.6079\ \overline{0.0574}\ 1.7564\rangle$	0.6018
$7.97°/\langle0\bar{1}1\bar{3}\rangle$			6.5°	4.7°	$8.0197°$ $/\langle0.0383\ \overline{0.6037}\ 0.5654\ \overline{1.7499}\rangle$	0.2703
$13.37°/\langle\bar{1}01\bar{3}\rangle$			10.8°	7.8°	$13.3154°$ $/\langle\overline{0.5514}\ \overline{0.0637}\ 0.6150\ \overline{1.7495}\rangle$	0.7373
$6.05°/\langle0\bar{1}12\rangle$	$\langle0001\rangle$	$\langle10\bar{1}0\rangle$	4.1°	4.4°	$6.0135°$ $/\langle\overline{0.0302}\ \overline{0.7152}\ 0.7454\ 1.4722\rangle$	0.1637
$6.29°/\langle02\bar{2}1\rangle$			1.4°	6.1°	$6.2584°$ $/\langle0.0137\ 0.9663\ \overline{0.9801}\ 0.4828\rangle$	0.0818
$5.03°/\langle0\bar{1}13\rangle$			4.1°	2.9°	$5.0216°$ $/\langle\overline{0.0238}\ \overline{0.5645}\ 0.5883\ 1.7634\rangle$	0.1141
$6.60°/\langle\bar{1}01\bar{1}\rangle$			2.8°	6.0°	$6.6206°$ $/\langle\overline{0.8920}\ \overline{0.0255}\ 0.9175\ \overline{0.9128}\rangle$	0.1494
$6.29°/\langle10\bar{1}\bar{2}\rangle$			4.3°	4.6°	$6.2960°$ $/\langle0.7134\ 0.0316\ \overline{0.7450}\ \overline{1.4746}\rangle$	0.1760
$13.99°/\langle\bar{1}011\rangle$			5.8°	12.7°	$13.9568°$ $/\langle\overline{0.9344}\ 0.0531\ 0.8813\ 0.8941\rangle$	0.6480

Table A2-4 Calculation results for low-angle boundaries with disorientation axis around $\langle11\bar{2}y\rangle$.

Experimental result $G^{ex}\ (\theta/T)^{ex}$	T_1	T_2	**Calculated result** θ_1	θ_2	$G\ (\theta/T)$	$\Delta\theta$
$5.53°/\langle\bar{1}2\bar{1}\bar{3}\rangle$			3.5°	4.3°	$5.5438°$ $/\langle\overline{0.4707}\ 0.8940\ \overline{0.4234}\ \overline{1.3632}\rangle$	0.1391
$10.38°/\langle11\bar{2}6\rangle$			8.8°	5.5°	$10.3745°$ $/\langle0.3457\ 0.2644\ \overline{0.6101}\ 1.8310\rangle$	0.4220
$5.46°/\langle\bar{1}2\bar{1}2\rangle$	$\langle0001\rangle$	$\langle11\bar{2}0\rangle$	2.6°	4.8°	$5.4586°$ $/\langle\overline{0.4869}\ 1.0137\ \overline{0.5268}\ 1.0284\rangle$	0.1137
$3.07°/\langle\bar{1}\bar{1}24\rangle$			2.2°	2.1°	$3.0413°$ $/\langle\overline{0.3848}\ \overline{0.4113}\ 0.7960\ \overline{1.5625}\rangle$	0.0573
$10.36°/\langle2\bar{1}\bar{1}2\rangle$			4.9°	9.1°	$10.3329°$ $/\langle1.0148\ \overline{0.5450}\ \overline{0.4698}\ 1.0223\rangle$	0.3914
$10.52°/\langle11\bar{2}1\rangle$			3.1°	10.1°	$10.5639°$ $/\langle0.5252\ 0.5769\ \overline{1.1021}\ 0.6323\rangle$	0.4717

We further simulated the combination of the two rotations θ_1/T_1 ($\theta_1 = 1-10°$; $T_1 = \langle0001\rangle$) and θ_2/T_2 ($\theta_2 = 1-10°$; $T_2 = \langle10\bar{1}0\rangle\ or\ \langle11\bar{2}0\rangle$) that produces a total rotation θ/T. The results are shown with the variation of θ as a function of θ_1 and θ_2 and with the stereographic projection of T as a function of the θ_1/θ_2 ratio in Fig. A2-2. When $T_2 = \langle10\bar{1}0\rangle$, it is seen that the two rotation angles θ_1 and θ_2 have a symmetrical contribution with respect to $\theta_1/\theta_2 = 1$ to the total disorientation angle. For the rotation axis, whatever the two rotations

$\theta_1/\langle 0001\rangle$ and $\theta_2/\langle 10\bar{1}0\rangle$, the total rotation axis always falls near the $\langle 10\bar{1}x\rangle$ line (the thick black line in Fig.A2-2 (a)) that runs from $\langle 0001\rangle$ to $\langle 10\bar{1}0\rangle$. Similar to the case of $\langle 10\bar{1}x\rangle$, when $T_2 = \langle 11\bar{2}0\rangle$ the combination of the two rotation angles also have a symmetrical contribution with respect to $\theta_1/\theta_2 = 1$ to the final disorientation angle, as shown in Fig. Fig. A2-2 (b). For the rotation axis, whatever the two rotations $\theta_1/\langle 0001\rangle$ and $\theta_2/\langle 11\bar{2}0\rangle$, the final rotation axis always fall near the $\langle 11\bar{2}y\rangle$ line (the thick black line in Fig. A2-2 (b)) that runs from $\langle 0001\rangle$ to $\langle 11\bar{2}0\rangle$.

The above results demonstrate that the extended IGMA approach is capable of revealing the mechanisms driving the evolution of the low-angle boundaries, when direct dislocation examination is not possible for the material.

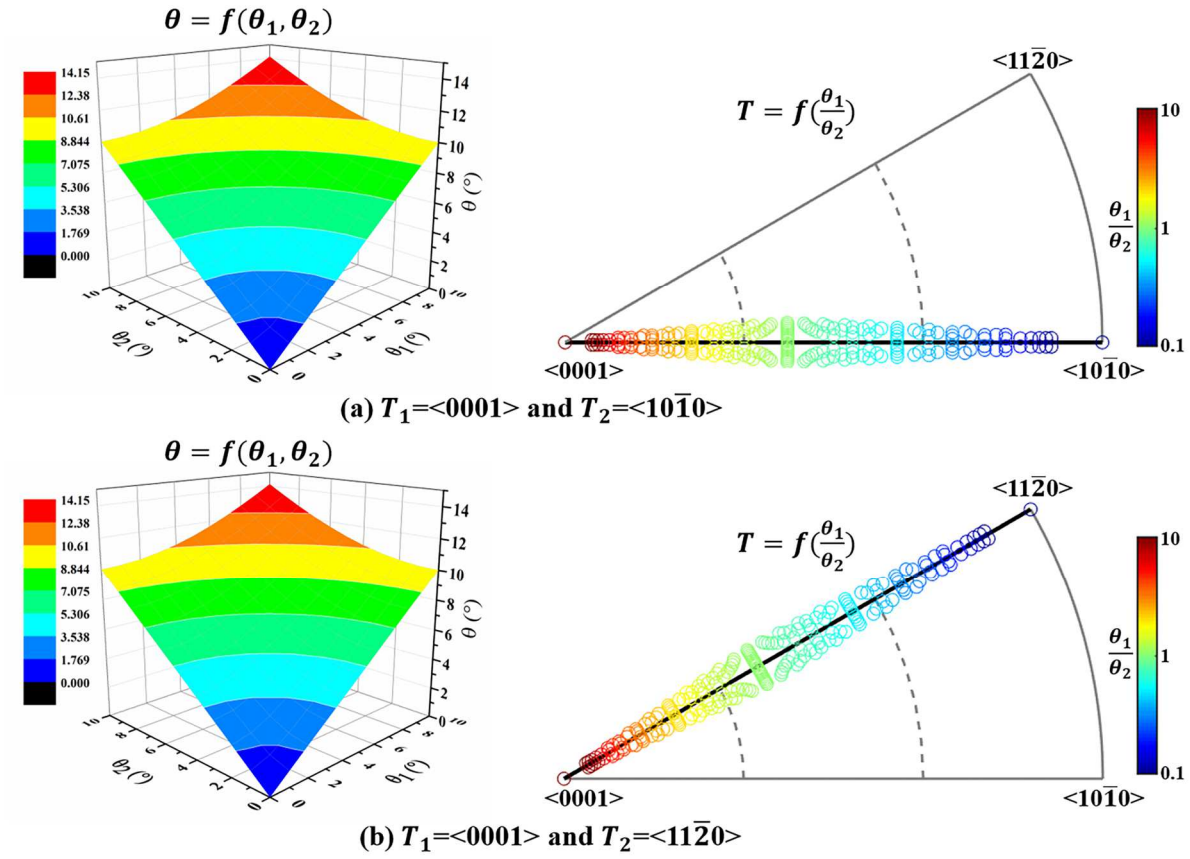

Fig. A2-2 Calculated disorientation of low-angle boundary, in terms of θ/T on function of the first rotation θ_1/T_1 ($T_1 = \langle 0001\rangle$) and the second rotation θ_2/T_2. (a) $T_2 = \langle 10\bar{1}0\rangle$; (b) $T_2 = \langle 11\bar{2}0\rangle$.

References

[1] A. Rollett, F. Humphreys, G.S. Rohrer, M. Hatherly, J. Humphreys, Gregory S. Rohrer, A. Rollett, F. Humphreys, G.S. Rohrer, M. Hatherly, Recrystallization and Related Annealing Phenomena, 3rd Editio, Elsevier Ltd, 2004. doi:10.1016/B978-0-08-044164-1.X5000-2.

[2] K. Huang, R.E. Logé, A review of dynamic recrystallization phenomena in metallic materials, Mater. Des. 111 (2016) 548–574. doi:10.1016/j.matdes.2016.09.012.

[3] T. Sakai, M. Ohashi, Dislocation substructures developed during dynamic recrystallisation in polycrystalline nickel, Mater. Sci. Technol. (United Kingdom). 6 (1990) 1251–1257. doi:10.1179/mst.1990.6.12.1251.

[4] D.G. Cram, H.S. Zurob, Y.J.M. Brechet, C.R. Hutchinson, Modelling discontinuous dynamic recrystallization using a physically based model for nucleation, Acta Mater. 57 (2009) 5218–5228. doi:10.1016/j.actamat.2009.07.024.

[5] T. Sakai, J.J. Jonas, Plastic Deformation: Role of Recovery and Recrystallization, Elsevier Ltd., 2016. doi:10.1016/b978-0-12-803581-8.03179-9.

[6] R.D. Doherty, D.A. Hughes, F.J. Humphreys, J.J. Jonas, D. Juul Jensen, M.E. Kassner, W.E. King, T.R. McNelley, H.J. McQueen, A.D. Rollett, Current issues in recrystallization: A review, Mater. Sci. Eng. A. 238 (1997) 219–274. doi:10.1016/S0921-5093(97)00424-3.

[7] T. Sakai, A. Belyakov, R. Kaibyshev, H. Miura, J.J. Jonas, Dynamic and post-dynamic recrystallization under hot, cold and severe plastic deformation conditions, Prog. Mater. Sci. 60 (2014) 130–207. doi:10.1016/j.pmatsci.2013.09.002.

[8] A.M. Wusatowska-Sarnek, H. Miura, T. Sakai, Nucleation and microtexture development under dynamic recrystallization of copper, Mater. Sci. Eng. A. (2002). doi:10.1016/S0921-5093(01)01336-3.

[9] A. Belyakov, H. Miura, T. Sakai, Dynamic recrystallization under warm deformation of a 304 type austenitic stainless steel, Mater. Sci. Eng. A. 255 (1998) 139–147. doi:10.1016/s0921-5093(98)00784-9.

[10] E. Brünger, X. Wang, G. Gottstein, Nucleation mechanisms of dynamic recrystallization in austenitic steel alloy 800H, Scr. Mater. 38 (1998) 1843–1849. doi:10.1016/S1359-6462(98)00124-9.

[11] A. Dehghan-Manshadi, M.R. Barnett, P.D. Hodgson, Recrystallization in AISI 304 austenitic stainless steel during and after hot deformation, Mater. Sci. Eng. A. 485 (2008) 664–672. doi:10.1016/j.msea.2007.08.026.

[12] D. Ponge, G. Gottstein, Necklace formation during dynamic recrystallization: Mechanisms and impact on flow behavior, Acta Mater. 46 (1998) 69–80. doi:10.1016/S1359-6454(97)00233-4.

[13] W. Roberts, B. Ahlblom, A nucleation criterion for dynamic recrystallization during hot working, Acta Metall. 26 (1978) 801–813. doi:10.1016/0001-6160(78)90030-5.

[14] S. Gourdet, F. Montheillet, A model of continuous dynamic recrystallization, Acta Mater. 51 (2003) 2685–2699. doi:10.1016/S1359-6454(03)00078-8.

[15] T. Sakai, H. Miura, A. Goloborodko, O. Sitdikov, Continuous dynamic recrystallization during the transient severe deformation of aluminum alloy 7475, Acta Mater. (2009). doi:10.1016/j.actamat.2008.09.001.

[16] F. Musin, A. Belyakov, R. Kaibyshev, Y. Motohashi, G. Itoh, K. Tsuzaki, Microstructure evolution in a cast 1421AI alloy during hot equal-channel angular extrusion, Rev. Adv. Mater. Sci. 25 (2010) 107–112.

[17] F. Appel, J.D.H. Paul, M. Oehring, Fritz Appel, Jonathan David Heaton Paul, Michael Oehring, Gamma Titanium Aluminide Alloys: Science and Technology, 2011. doi:10.1002/9783527636204.

[18] X. Yang, Y. Okabe, H. Miura, T. Sakai, Effect of prior strain on continuous recrystallization in AZ31 magnesium alloy after hot deformation, Mater. Sci. Eng. A. 535 (2012) 209–215. doi:10.1016/j.msea.2011.12.066.

[19] Y. Yang, X. Yang, Z. Xiao, D. Zhang, J. Wang, T. Sakai, Annealing behavior of a cast Mg-Gd-Y-Zr alloy with necklace fine grains developed under hot deformation, Mater. Sci. Eng. A. 688 (2017) 280–288. doi:10.1016/j.msea.2017.02.008.

[20] X. Yang, Z. Ji, H. Miura, T. Sakai, Dynamic recrystallization and texture development during hot deformation of magnesium alloy AZ31, Trans. Nonferrous Met. Soc. China (English Ed. 19 (2009) 55–60. doi:10.1016/S1003-6326(08)60228-9.

[21] X. Yang, H. Miura, T. Sakai, Dynamic nucleation of new grains in magnesium alloy during hot deformation, Mater. Sci. Forum. 419–422 (2003) 515–520. doi:10.4028/www.scientific.net/msf.419-422.515.

[22] H. Miura, M. Ito, X. Yang, J.J. Jonas, Mechanisms of grain refinement in Mg-6Al-1Zn alloy during hot deformation, Mater. Sci. Eng. A. 538 (2012) 63–68. doi:10.1016/j.msea.2012.01.014.

[23] O. Sitdikov, R. Kaibyshev, Dynamic recrystallization in pure magnesium, Mater. Trans. 42 (2001) 1928–1937. doi:10.2320/matertrans.42.1928.

[24] M.R. Barnett, Z. Keshavarz, A.G. Beer, D. Atwell, Influence of grain size on the compressive deformation of wrought Mg-3Al-1Zn, Acta Mater. 52 (2004) 5093–5103. doi:10.1016/j.actamat.2004.07.015.

[25] A. Galiyev, R. Kaibyshev, G. Gottstein, Correlation of plastic deformation and dynamic recrystallization in magnesium alloy ZK60, Acta Mater. 49 (2001) 1199–1207. doi:10.1016/S1359-6454(01)00020-9.

[26] H. Miura, X. Yang, T. Sakai, H. Nogawa, S. Miura, Y. Watanabe, J.J. Jonas, High temperature deformation and extended plasticity in Mg single crystals, Philos. Mag. 85 (2005) 3553–3565. doi:10.1080/14786430500228440.

[27] Q. Chao, H. Beladi, I. Sabirov, P.D. Hodgson, Deformation behaviour of a commercial pure titanium alloy during hot compression testing, Mater. Sci. Forum. 773–774 (2014) 281–286. doi:10.4028/www.scientific.net/MSF.773-774.281.

[28] Z. Zeng, Y. Zhang, S. Jonsson, Deformation behaviour of commercially pure titanium during simple hot compression, Mater. Des. 30 (2009) 3105–3111. doi:10.1016/j.matdes.2008.12.002.

[29] C. Yan, A. Feng, S. Qu, J.L. Sun, J. Shen, Hot deformation and grain refinement mechanisms of commercially pure titanium processed via three-directional cryo-compression, Mater. Sci. Eng. A. 731 (2018) 266–277. doi:10.1016/j.msea.2018.06.058.

[30] D.W. James, D.M. Moon, The Science, Technology and Application of Titanium, 1970. doi:10.1016/B978-0-08-006564-9.50083-X.

[31] E. Schwaighofer, H. Clemens, J. Lindemann, A. Stark, S. Mayer, Hot-working behavior of an advanced intermetallic multi-phase γ-TiAl based alloy, Mater. Sci. Eng. A. 614 (2014) 297–310. doi:10.1016/j.msea.2014.07.040.

[32] T. Schmoelzer, K.D. Liss, C. Kirchlechner, S. Mayer, A. Stark, M. Peel, H. Clemens, An in-situ high-energy X-ray diffraction study on the hot-deformation behavior of a β-phase containing TiAl alloy, Intermetallics. 39 (2013) 25–33. doi:10.1016/j.intermet.2013.02.016.

[33] K.D. Liss, T. Schmoelzer, K. Yan, M. Reid, M. Peel, R. Dippenaar, H. Clemens, In situ study of dynamic recrystallization and hot deformation behavior of a multiphase titanium aluminide alloy, J. Appl. Phys. 106 (2009) 113526. doi:10.1063/1.3266177.

[34] S.R. Dey, A. Hazotte, E. Bouzy, Crystallography and phase transformation mechanisms in TiAl-based alloys - A synthesis, Intermetallics. 17 (2009) 1052–1064. doi:10.1016/j.intermet.2009.05.013.

[35] L. Germain, N. Gey, R. Mercier, P. Blaineau, M. Humbert, An advanced approach to reconstructing parent orientation maps in the case of approximate orientation relations: Application to steels, Acta Mater. 60 (2012) 4551–4562. doi:10.1016/j.actamat.2012.04.034.

[36] Y.B. Chun, M. Battaini, C.H.J. Davies, S.K. Hwang, Distribution characteristics of in-grain Misorientation axes in cold-rolled commercially pure titanium and their correlation with active slip modes, Metall. Mater. Trans. A. 41 (2010) 3473–3487. doi:10.1007/s11661-010-0410-4.

[37] Y.B. Chun, C.H.J. Davies, Investigation of prism <a> slip in warm-rolled AZ31 alloy, Metall. Mater. Trans. A. 42 (2011) 4113–4125. doi:10.1007/s11661-011-0800-2.

[38] J.P. Hadorn, K. Hantzsche, S. Yi, J.A.N. Bohlen, D. Letzig, J.A. Wollmershauser, S.R. Agnew, Role of solute in the texture modification during hot deformation of Mg-rare earth alloys, Metall. Mater. Trans. A. 43 (2012) 1347–1362. doi:10.1007/s11661-011-0923-5.

[39] M. Yamasaki, K. Hagihara, S.I. Inoue, J.P. Hadorn, Y. Kawamura, Crystallographic classification of kink bands in an extruded Mg-Zn-Y alloy using intragranular misorientation axis analysis, Acta Mater. 61 (2013) 2065–2076. doi:10.1016/j.actamat.2012.12.026.

[40] R. Maddin, N.K. Chen, Geometrical aspects of the plastic deformation of metal single crystals, Prog. Met. Phys. 5 (1954) 53–95. doi:10.1016/0502-8205(54)90004-0.

[41] S.L.S. S. Mironov, M. Murzinova, S. Zherebtsov, G.A. Salishchev, S. Mironov, M. Murzinova, S. Zherebtsov, G.A. Salishchev, S.L. Semiatin, Microstructure evolution during warm working of Ti–6Al–4V with a colony-α microstructure, Acta Mater. 57 (2009) 2470–2481. doi:10.1016/j.actamat.2009.02.016.

[42] E. Schwaighofer, H. Clemens, S. Mayer, J. Lindemann, J. Klose, W. Smarsly, V. Güther, Microstructural design and mechanical properties of a cast and heat-treated intermetallic multi-phase γ-TiAl based alloy, Intermetallics. 44 (2014) 128–140. doi:10.1016/j.intermet.2013.09.010.

[43] Addressing pseudo-symmetric mis-indexing in the EBSD analysis of gamma-TiAl, (n.d.). https://nano.oxinst.com/campaigns/downloads/addressing-pseudo-symmetric-mis-indexing.

[44] Grain size and grain boundary characterisation in SEM, (n.d.). https://ebsd.com/solving-problems-with-ebsd/grain-size-and-grain-boundary-characterisation-in-sem.

[45] J.K. Mackenzie, Second paper on statistics associated with the random disorientation of cubes, Biometrika[1] J.K. Mackenzie, Second Pap. Stat. Assoc. with Random Disorientation Cubes, Biometrika. 45 229–240. Doi10.1093/Biomet/45.1-2.229. 45 (1958) 229–240. doi:10.1093/biomet/45.1-2.229.

[46] P.G. Partridge, The crystallography and deformation modes of hexagonal close-packed metals, Metall. Rev. 12 (1967) 169–194. doi:10.1179/mtlr.1967.12.1.169.

[47] T.B. Britton, F.P.E. Dunne, A.J. Wilkinson, On the mechanistic basis of deformation at the microscale in hexagonal close-packed metals, Proc. R. Soc. A Math. Phys. Eng. Sci. 471 (2015) 20140881. doi:10.1098/rspa.2014.0881.

[48] H.W. Son, J.W. Lee, S.K. Hyun, Mechanism of grain boundary serration during hot deformation of AZ31 alloy: Role of grain boundary dislocations and grain boundary sliding, Int. J. Plast. 125 (2020) 118–132. doi:10.1016/j.ijplas.2019.09.003.

[49] T.R. Bieler, S.L. Semiatin, The origins of heterogeneous deformation during primary hot working of Ti-6Al-4V, Int. J. Plast. 18 (2002) 1165–1189. doi:10.1016/S0749-6419(01)00057-2.

[50] P.R. Rios, F. Siciliano, H.R.Z. Sandim, R.L. Plaut, A.F. Padilha, Nucleation and growth during recrystallization, Mater. Res. 8 (2005) 225–238. doi:10.1590/S1516-14392005000300002.

Figure captions:

Fig. 1 Initial microstructure. (a_1) EBSD Y axis inverse pole figure (Y-IPF) micrograph of the reconstructed high-temperature α phase; (a_2) EBSD band quality indexed micrograph before reconstruction; (b) disorientation angle distribution of α phase.

Fig. 2 Deformed high-temperature α microstructure at true strain of 0.05. (a_1) EBSD Y axis inverse pole figure (IPF) micrograph of α phase; (a_2) original EBSD micrograph with band quality indexed contrast. The black lines stand for grain boundaries and the red lines for the bulged boundaries. (b) Kernel average misorientation (KAM) micrograph of (a_1). In the figures, load direction (LD) is parallel to Y axis (the same below).

Fig. 3 (a) EBSD Y axis IPF micrograph of a representative example of boundary bulge regions and the correlated disorientations (in angle and axis) along L1 in grain G1. (b) Prismatic slip plane and direction ($\{1\bar{1}00\}$ and $<11\bar{2}0>$) pole figures of G1. (c) Illustration of low-angle boundary formed by edge prismatic <a> dislocations characterized by a rotation around $\langle 000\bar{1}\rangle$ and a boundary plane of $\{11\bar{2}0\}$.

Fig. 4 Schema illustrating the formation of boundary bulging by dislocation slip and the formation of symmetric-tilt low-angle boundary by dynamic recovery (DRV). (a) Grain boundary broadening; (b) activation of dislocation slip and dislocation pile-ups in front of broadened boundary; (c) annihilation of dislocations at grain boundary and formation of boundary bulge; (d) rearrangement of dislocations to form symmetrical-tilt low-angle boundary.

Fig. 5 Microstructural and crystallographic features of α grains in specimen deformed to true strain of 0.07. (a) EBSD Y axis IPF micrograph of high-temperature α phase; (b) EBSD Y axis IPF micrograph of the area outlined with blue rectangle in (a), and pole figures of prismatic slip plane and direction ($\{1\bar{1}00\}$ and $\langle 11\bar{2}0\rangle$) and the disorientation axis $\langle\bar{1}011\rangle$ in G1; (c) EBSD Y axis IPF micrograph of the area outlined with black rectangle in (a), and pole figures of prismatic slip plane and direction ($\{1\bar{1}00\}$ and $\langle 11\bar{2}0\rangle$) and the disorientation axis $\langle 11\bar{2}1\rangle$ in G2.

Fig. 6 Schema illustrating the evolution of low-angle boundaries with further deformation. (a) Asymmetrical-tilt boundaries with disorientation of θ/T ($T = \langle 10\bar{1}x\rangle$) formed by the first rotation θ_1/T_1 ($T_1 = \langle 000\bar{1}\rangle$) and the second rotation θ_2/T_2 ($T_2 = \langle 1\bar{1}00\rangle$); (b) tilt-twist boundary with the disorientation of θ/T ($T = \langle 11\bar{2}y\rangle$) formed by the first rotation θ_1/T_1 ($T_1 = \langle 0001\rangle$) and the second rotation θ_2/T_2 ($T_2 = \langle 11\bar{2}0\rangle$).

Fig. 7 Micrographs of the α phase in the specimen deformed to the true strain of 0.29. (a) EBSD Y axis IPF micrograph; (b) KAM micrograph.

Fig. 8 EBSD Y axis IPF micrographs and the corresponding $\{0001\}$ and $\{10\bar{1}0\}$ pole figures of the grains in two necklace regions. (a) Necklace region with less small grains representing the beginning of grain detachment; (b) necklace region with more small grains representing

the mixing of small grains. The poles in the pole figures in (b) are from the coarse red grain and the small red domains.

Fig. 9 EBSD Y axis IPF micrograph of the specimen deformed to the true strain of 1.05.

Fig. A1 Original EBSD micrographs with band quality indexed contrast of the specimens deformed to true strains of (a) 0.07, (b) 0.29, and (c) 1.05.

Fig. A2-1 (a) Schema illustrating the decomposition of the low-angle boundary into two symmetrical tilt boundaries made of dislocation with two different Burgers vectors or into one symmetrical-tilt boundary and a rotational sliding around the axis normal to the extra-half plane of the dislocation of symmetrical-tilt boundary; (b) schema showing the corresponding crystallographic rotations.

Fig. A2-2 Calculated disorientation of low-angle boundary, in terms of *θ/T* on function of the first rotation θ_1/T_1 ($T_1 = \langle 0001 \rangle$) and the second rotation θ_2/T_2. (a) $T_2 = \langle 10\bar{1}0 \rangle$; (b) $T_2 = \langle 11\bar{2}0 \rangle$.